

PAPER

## Nanoporous anodic aluminum oxide as a promising material for the electrostatically-controlled thin film interference filter

To cite this article: Pei-Hsuan Lo *et al* 2015 *J. Micromech. Microeng.* **25** 025001

View the [article online](#) for updates and enhancements.

### Related content

- [Broad-band anti-reflective pore-like sub-wavelength surface nanostructures on sapphire for optical windows](#)  
Zhao-Qing Lin, Gui-Gen Wang, Ji-Li Tian *et al.*
- [Novel RF MEMS capacitive switches with design flexibility for multi-frequency operation](#)  
Sarath Gopalakrishnan, Amitava DasGupta and Deleep R Nair
- [A grayscale pneumatic micro-valve for use in a reconfigurable tactile tablet for vision-impaired individuals](#)  
Joseph Devin Schneider, Jovan David Rebolledo-Mendez and Shamus McNamara



**IOP | ebooks™**

Bringing you innovative digital publishing with leading voices to create your essential collection of books in STEM research.

Start exploring the collection - download the first chapter of every title for free.

# Nanoporous anodic aluminum oxide as a promising material for the electrostatically-controlled thin film interference filter

Pei-Hsuan Lo<sup>1</sup>, Guo-Lun Luo<sup>2</sup>, Chih-Chun Lee<sup>1</sup> and Weileun Fang<sup>1,2</sup>

<sup>1</sup> Institute of NanoEngineering and MicroSystems, National Tsing Hua Univ., Hsinchu, Taiwan

<sup>2</sup> Power Mechanical Engineering, National Tsing Hua Univ., Hsinchu, Taiwan

E-mail: [fang@pme.nthu.edu.tw](mailto:fang@pme.nthu.edu.tw)

Received 23 June 2014, revised 29 September 2014

Accepted for publication 6 October 2014

Published 15 January 2015



CrossMark

## Abstract

This study presents the approach to implement the electrostatically-controlled thin film optical filter by using a nanoporous anodic aluminum oxide (np-AAO) layer as the key suspended micro structure. The bi-stable optical filter operates in the visible spectral range. In this work, the presented bi-stable optical filter has averaged reflectivity of 60%, and the central wavelengths are 580 and 690 nm respectively for on and off states. The presented np-AAO layer offers the following merits for the thin film optical filter: (1) material properties of np-AAO film, such as refractive index, elastic modulus and dielectric constant, can be easily changed by a low temperature pore-widening process, (2) in-use stiction of the suspended np-AAO structure can be reduced by the small contact area of nanoporous textures, (3) driving (pull-in) voltage can be reduced due to a large dielectric constant ( $\epsilon_{AAO}$  is 7.05) and small stiffness of np-AAO film and (4) dielectric charging can be reduced by the np-AAO material; thus the offset voltage is small. The study reports the design, fabrication and experimental results of the bi-stable optical filter to demonstrate the advantages of the presented device. The np-AAO material also has the potential for applications of other electrostatic drive micro devices.

Keywords: thin film, optical filter, nanoporous anodic aluminum oxide (np-AAO), stiction, dielectric charge

(Some figures may appear in colour only in the online journal)

## 1. Introduction

The microfabrication technologies have been employed to develop various interference-based optical MEMS devices for light modulation [1–10]. The MEMS optical interference filter has been developed to act as the wavelength selective switch for the application of color pixels [1–3], optical communication systems [4], interferometer [5–7], spectrometers [8, 9] and pressure sensors [10]. Due to the applications in multimode optical communications [5], the existing optical filters are mainly designed in the near infrared region. Currently, the applications of optical filters

have been extended to the visible-light range, such as panel display [1–3], biochemical analysis [9], microspectrometers [8], etc.

In general, the electrostatic actuation technique has the advantages of lower driving power and relative ease for microfabrication. Thus, the MEMS optical filters in [1–8] are driven by the electrostatic actuation. Nevertheless, the electric charging effect on the dielectric films is a critical concern for the electrostatic actuation approach [11]. The dielectric charging effect not only causes the non-linear electro-optical response, but also affects the reliability of the device. Furthermore, as reported in [1–3], the suspended MEMS structure will contact

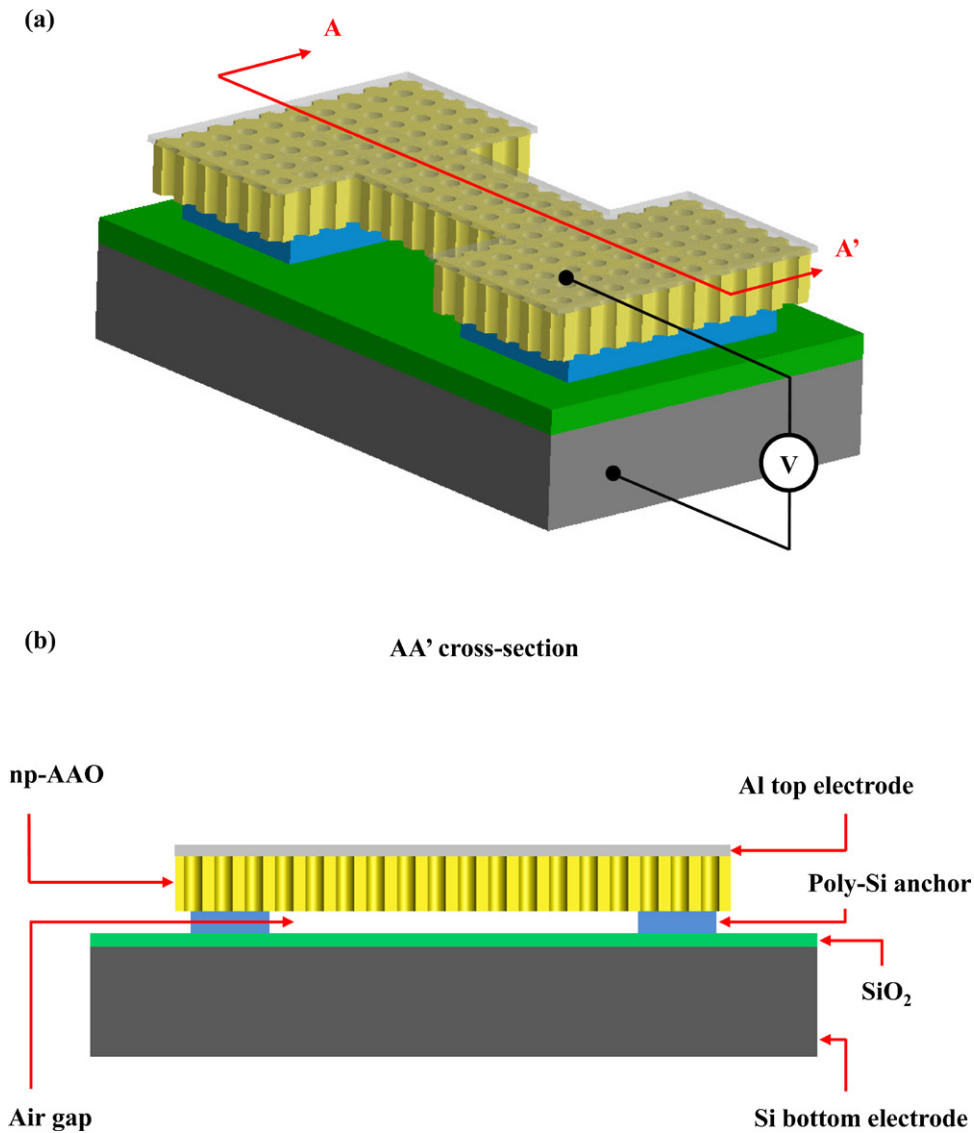


**Figure 1.** (a) The structure design of the proposed optical thin film filter and (b) the AA' cross section shows the composition of a multi-layered filter.

with the substrate surface for the bi-stable modulation optical filter while in use. Thus, the adhesion between suspended MEMS structures and the substrate becomes a critical failure mechanism and design consideration for the optical filters. Several approaches have been discussed to reduce the stiction between contact interfaces. For example, the surface with a nanodot-patterned texture has been exploited to reduce the surface adhesion [12]. However, complicated fabrication processes are required to prepare the structure. The anti-stiction layer coated onto the suspended MEMS structure, by using the atomic layer deposition (ALD) process, has also been reported [13]. This approach requires a higher temperature (300–500 °C) so as to limit its process compatibility. Moreover, the optical properties of the thin films to form the suspended MEMS structure are also important to the performance of the filter. As discussed in [14], the MEMS structure featured with high transparency in the applied wavelengths region is preferred.

The aforementioned design considerations for the MEMS optical filter can be improved by selecting the proper thin film materials utilizing simple microfabrication processes. Thus, the current study extends the concept in [15, 16] to the design and implementation of the bi-stable MEMS optical filter using the transparent nanoporous anodic aluminum oxide (np-AAO) film. The np-AAO film is a promising material and has found many current applications [17–21]. As reported in [15, 16], the np-AAO with hexagonally arranged nanopores is exploited to act as a template to implement 1D nanostructured materials including nanopillars, nanowires and nanodot arrays. The optical filters to control the interferometric property, by adjusting the pore size of np-AAO, are reported in [15, 22]. Moreover, the optical characteristics of np-AAO film are also investigated. In this study, the proposed bi-stable optical filter consisting of np-AAO film is driven by the electrostatic force. The driving voltage of the proposed MEMS optical filter is reduced by the high dielectric constant of np-AAO film [16].

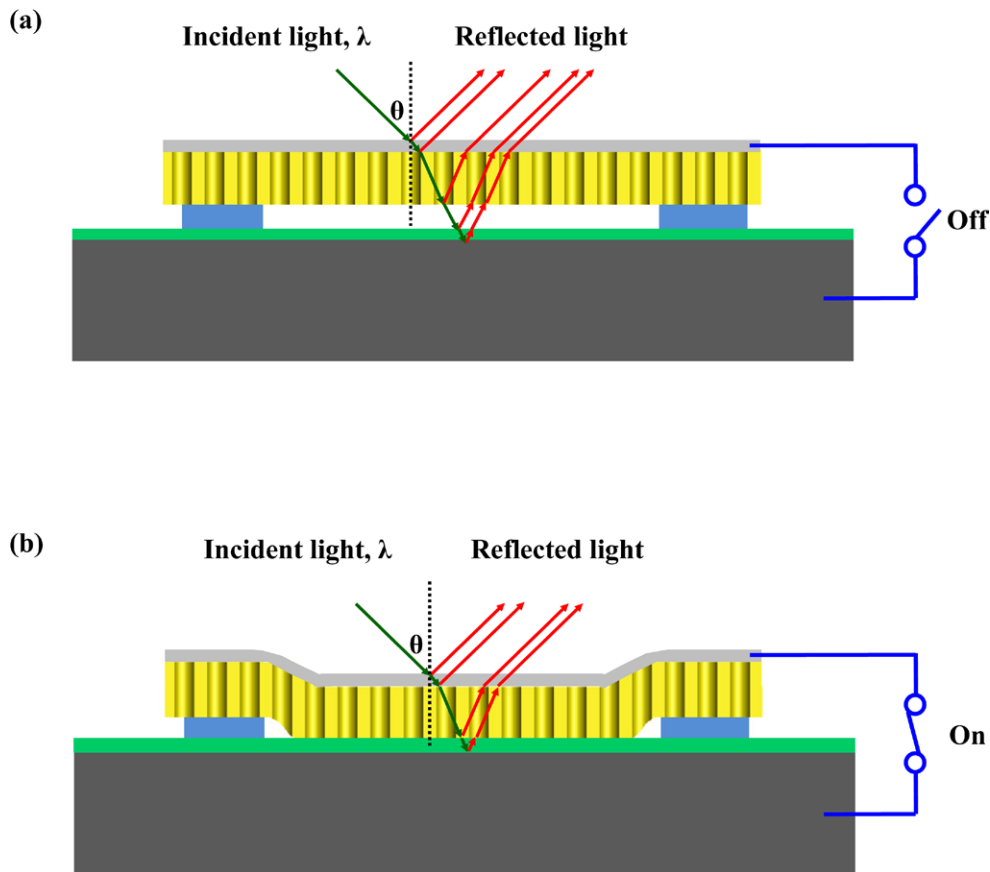


**Figure 2.** The operation mechanism of the proposed bi-stable optical filter, (a) off-state: the np-AAO film suspended on the substrate before applying voltage, and (b) on-state: the np-AAO film contact with the substrate after applying a pull-in dc voltage.

In addition, the np-AAO film with nanoporous texture is arranged as the contact interface to reduce the contact area. Thus, the stiction of suspended MEMS structure is prevented. It is easy to integrate the low temperature process for np-AAO film with other fabrication processes.

## 2. Concept and design

Figure 1(a) exhibits the structure design of the proposed optical thin film filter. The fixed-fixed beam is suspended on the Si substrate. The cross-sectional schematic plot in figure 1(b) also indicates the composition of multi layers of thin film filter. The Al thin film (20 nm) on top of the np-AAO layer is employed as the top electrode and optical reflector. The suspended and deformable np-AAO structure (350 nm) is employed to support the thin Al film and also act as the electrical isolation layer. The polysilicon (poly-Si) anchor acts as the spacer to define the air gap between the np-AAO layer and substrate. The silicon substrate is exploited as the bottom electrode and also the optical reflector. Note that the thermal oxide is an etching protection layer for Si substrate. The suspended np-AAO film will be deformed by the electrostatic force after input voltage. Thus, the Si substrate reflector is fixed, while the Al film reflector is deformable for the wavelength modulation. Figure 2 shows the operation mechanism of the optical thin film filter. Figure 2(a) shows the np-AAO film suspended on the substrate with an air gap before applying

voltage. When the dc operation voltage is applied on the Al film, the pull-in of flexible np-AAO film will be achieved by the electrostatic force between the top and bottom electrodes, as indicated in figure 2(b). As the light beam is incident onto a substrate with thin films of different materials, multiple transmission and reflections will take place at each interface [23]. Thus, figures 2(a) and 2(b) also respectively display the light beams reflected by the bi-stable multi-layers of thin film filter. The interference between the reflected light beams of different optical path length will occur. Thus, the characteristic of reflected light beam will be influence by the thickness and material characteristics (e.g. refractive index  $n$ ) of thin films for the presented multi-layer optical device. In addition, the characteristic of reflected light beam can also be modulated by adjusting the air gap using electrostatic force.

The material properties of np-AAO film are influenced by the porosity  $P$ . The porosity  $P$  of the nano-honeycomb structure is the ratio of the pore area to the total area in a unit cell. As indicated in figure 3(a), the porosity determined from the geometry of the unit cell of the nano-honeycomb structure is expressed as [24],

$$P = \frac{2\pi}{\sqrt{3}} \left( \frac{r}{\rho} \right)^2 \quad (1)$$

where  $r$  is the pore radius and  $\rho$  is the interpore distance. The refractive index of np-AAO film can be further determined by the porosity  $P$  [25],

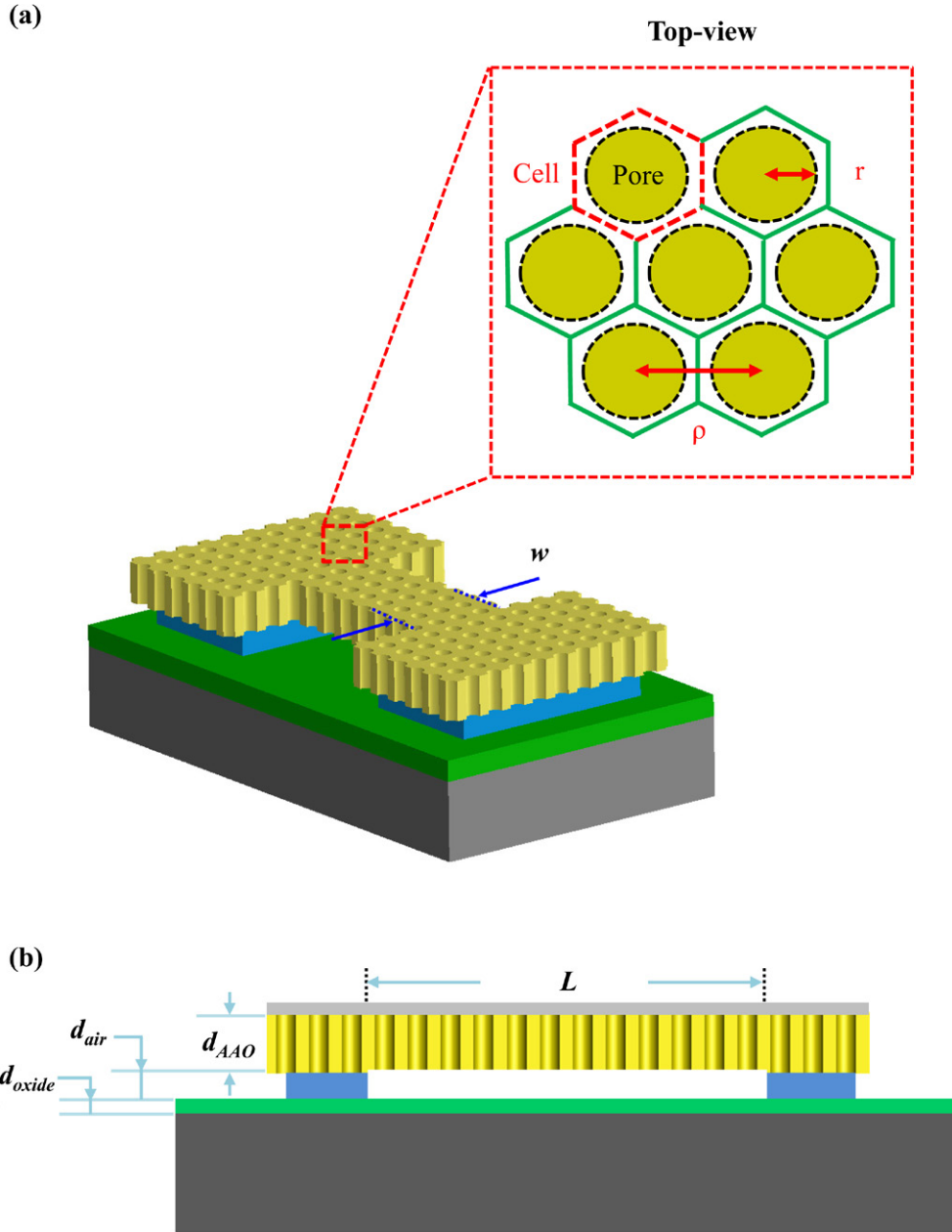


**Figure 3.** Schematic illustration shows the top-view and cross-section of the filter with nanopore structure.

$$n^2_{AAO} = (n_{Al_2O_3}^2 - 1)(1 - P) + 1 \quad (2)$$

where  $n_{AAO}$  and  $n_{Al_2O_3}$  are refractive indices of AAO film and  $Al_2O_3$ , respectively. In this study, the np-AAO film with superior dielectric constant is exploited to reduce actuation voltage. According to the model in [26], the pull-in voltage ( $V_{Pull-in}$ ) for the suspended MEMS structure can be expressed as,

$$V_{Pull-in} = \sqrt{\frac{8}{27} \frac{k d_{eff}^3}{\epsilon_0 \epsilon_{eff} A}} \quad (3)$$

where  $\epsilon_0$  is permittivity of air,  $\epsilon_{eff}$  denotes the effective relative dielectric constant of the isolation layers,  $A$  is the overlap area of the driving electrodes,  $k$  is the stiffness of suspended MEMS structure and  $d_{eff}$  represents the physical separation

between the driving electrodes. Thus, for the proposed suspended fixed-fixed beam design shown in figure 3(b), the  $V_{Pull-in}$  in equation (3) can be rewritten as,

$$V_{Pull-in} = \frac{32}{3} \sqrt{\frac{E_{AAO} I_{AAO} d_{eff}^3}{\epsilon_0 \epsilon_{eff} L^4 w}} \quad (4)$$

where  $E_{AAO}$ ,  $I_{AAO}$ ,  $L$  and  $w$  are respectively the Young's modulus, moment of inertia, length and width of the suspended fixed-fixed beam. Note that the thickness of Al film is much smaller than that of the np-AAO (20 versus 350nm) and thus the stiffness of the fixed-fixed beam is dominated by the np-AAO layer. To simplify the simulation model, the Al layer was ignored for the beam stiffness in equation (4). As reported

**Table 1.** Summary of the material properties and pull-in voltages of the optical filters consisting of different suspended materials.

| Specifications  | np-AAO    | np-AAO     | SiO <sub>2</sub>        | Si <sub>3</sub> N <sub>4</sub> |
|---|-----------|------------|-------------------------|--------------------------------|
| Porosity (%)  | 60        | 20         | N/A                     | N/A                            |
| Young's modulus, $E$ (GPa)  | 59.2 [27] | 236.8 [27] | 68 [28]                 | 320 [28]                       |
| Moment of inertia, $I$ ( $\mu\text{m}^4$ )                            | 0.071     | 0.143      | 0.179                   | 0.179                          |
| Length of the beam, $L$ ( $\mu\text{m}$ )                             |           |            | 110                     |                                |
| Separation between the electrodes, $d_{\text{eff}}$ ( $\mu\text{m}$ ) |           |            | 1.85                    |                                |
| Permittivity of air, $\epsilon_0$ (F/m)                               |           |            | $8.854 \times 10^{-12}$ |                                |
| Relative dielectric constant, $\epsilon$                              | 7.05      | 7.39       | 3.9 [28]                | 7.5 [28]                       |
| Effective relative dielectric constant, $\epsilon_{\text{eff}}$       | 2.29      | 2.3        | 2.18                    | 2.30                           |
| Actuation area, $A$ ( $\mu\text{m}^2$ )                               |           |            | $110 \times 50$         |                                |
| Pull-in voltage, $V$ (V)  | 4.5       | 12.8       | 7.8                     | 16.6                           |

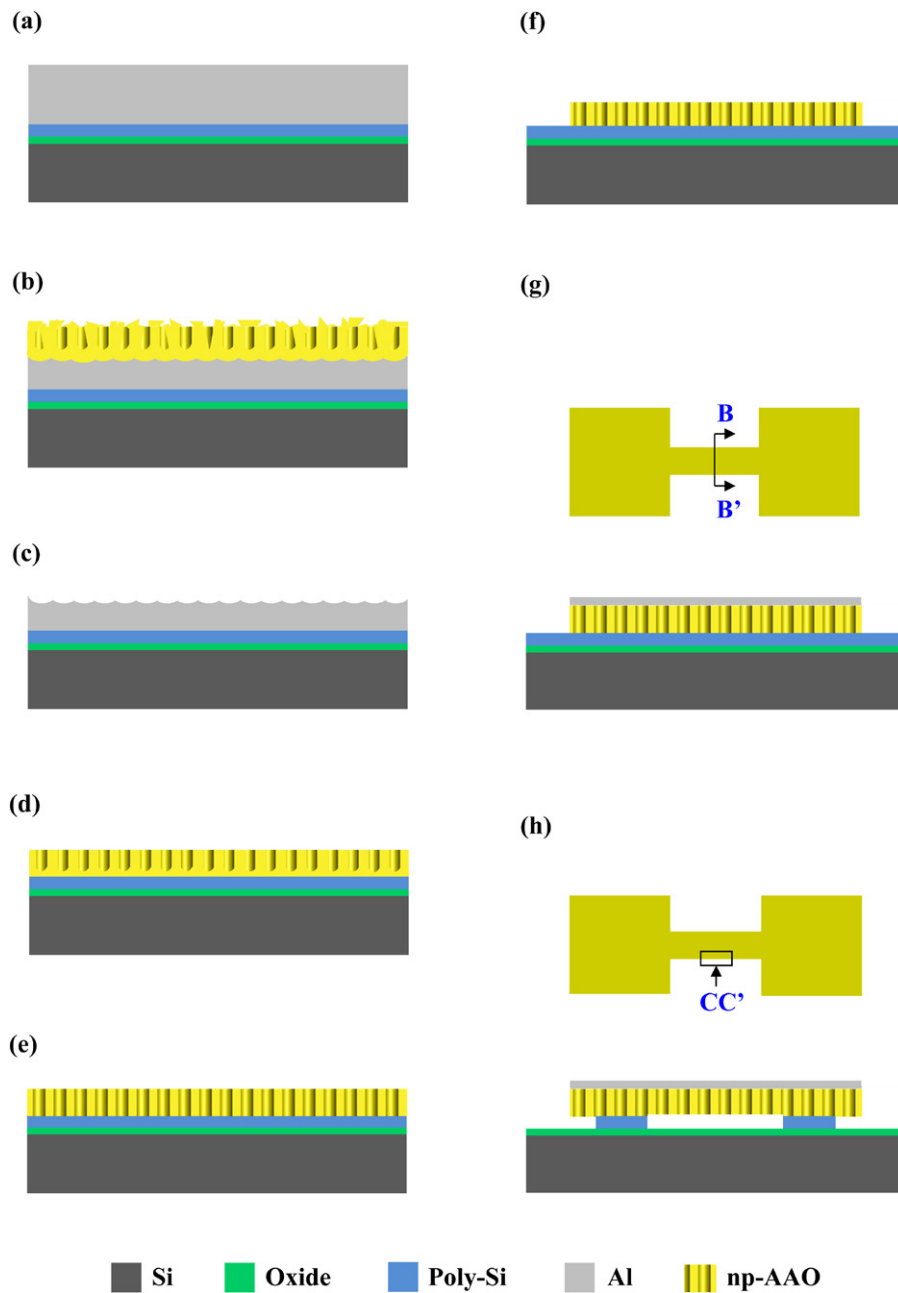


**Figure 4.** Fabrication process steps of the current optical thin film filter: (a) oxide/poly-Si and Al deposition on Si substrate, (b–f) growth and pattern of np-AAO film, (g) deposition of Al top electrode and (h) release of np-AAO beam.

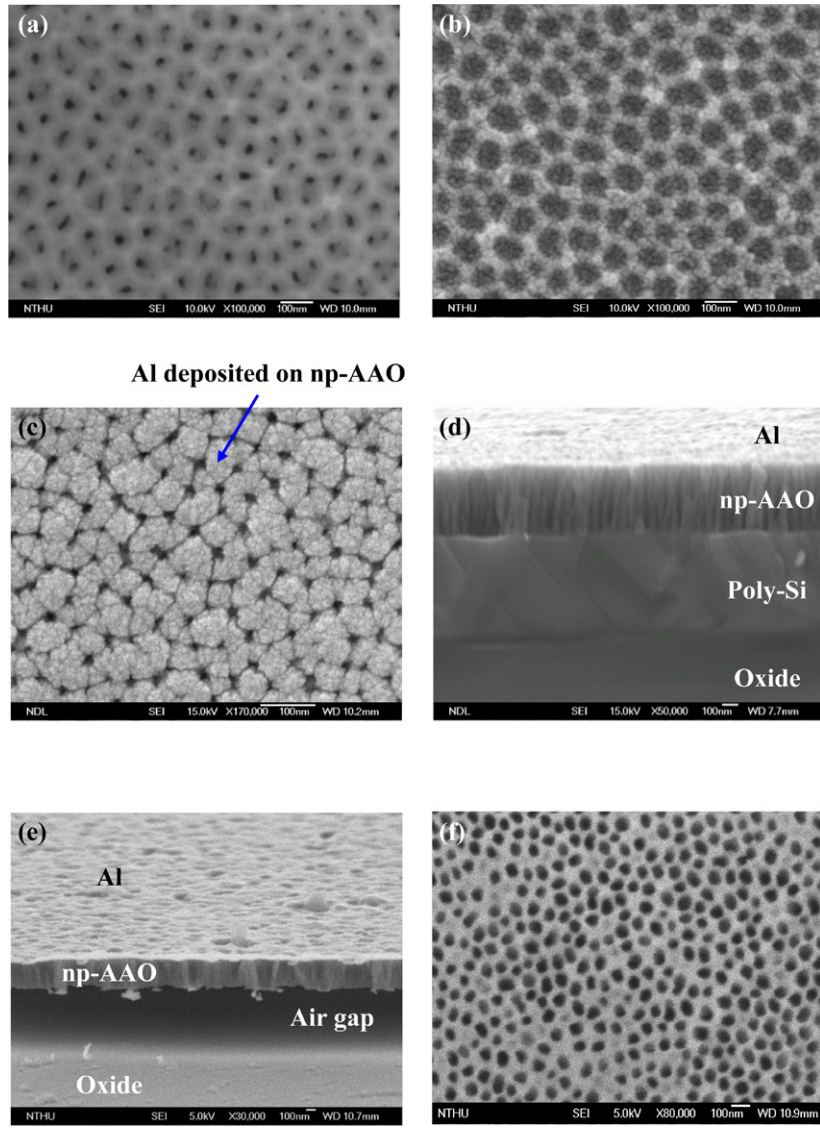


**Figure 5.** FE-SEM images of (a–b) top-view of np-AAO films with nanopores of different size, (c) np-AAO covered with Al film, (d) typical layers stacking of the device before the removal of poly-Si sacrificial layer, (e) np-AAO layer suspended on the substrate after the removal of poly-Si sacrificial layer and (f) morphology of the back side of np-AAO film.

in [24], the moment of inertia of the np-AAO beam with porosity of  $P$  is expressed as,

$$I_{AAO} = \frac{wd_{AAO}^3}{12} (1 - P) \quad (5)$$

where  $d_{AAO}$  is the thicknesses of the np-AAO film. Moreover, the effective relative dielectric constant  $\epsilon_{eff}$  of the isolation layers shown in figure 3(b) can be further expressed as,

$$\epsilon_{eff} = \frac{(d_{AAO} + d_{air} + d_{oxide})}{\frac{d_{AAO}}{\epsilon_{AAO}} + \frac{d_{air}}{\epsilon_{air}} + \frac{d_{oxide}}{\epsilon_{oxide}}} \quad (6)$$

where  $\epsilon_{AAO}$ ,  $\epsilon_{air}$  and  $\epsilon_{oxide}$  respectively denote the dielectric constants of the np-AAO film, air and oxide layer and  $d_{air}$  and  $d_{oxide}$  respectively denote the thicknesses of the air gap and oxide layer. The physical separation  $d_{eff}$  between the driving electrodes shown in figure 3(b) is,

$$d_{eff} = (d_{AAO} + d_{air} + d_{oxide}) \quad (7)$$

Based on the prediction from equations (3)–(7), the pull-in (driving) voltages of the optical filters consisting of different suspended materials, are summarized in table 1. It indicates that the dielectric constant, stiffness and pull-in voltage of the structure with np-AAO vary with the porosity. Note that Young’s modulus of np-AAO film decreases from 236.8 to 59.2GPa when its porosity increases from 20% to 60%, as predicted from [27]. The comparison of pull-in voltages among the np-AAO, oxide and nitride structures are also provided in table 1. The pull-in voltage is significantly reduced by increasing the porosity of the np-AAO film. In addition, after the formation of porous structure for np-AAO, the contact area  $A_{contact}$  of the beam with the substrate (by pull-in effect) will be reduced to,

$$(A_{contact})_{AAO} = A_{contact} (1 - P) \quad (8)$$

Thus, the adhesion force at the contact surface is reduced to prevent the stiction of the suspended beam. In summary, the np-AAO thin film exhibits good optical, mechanical and

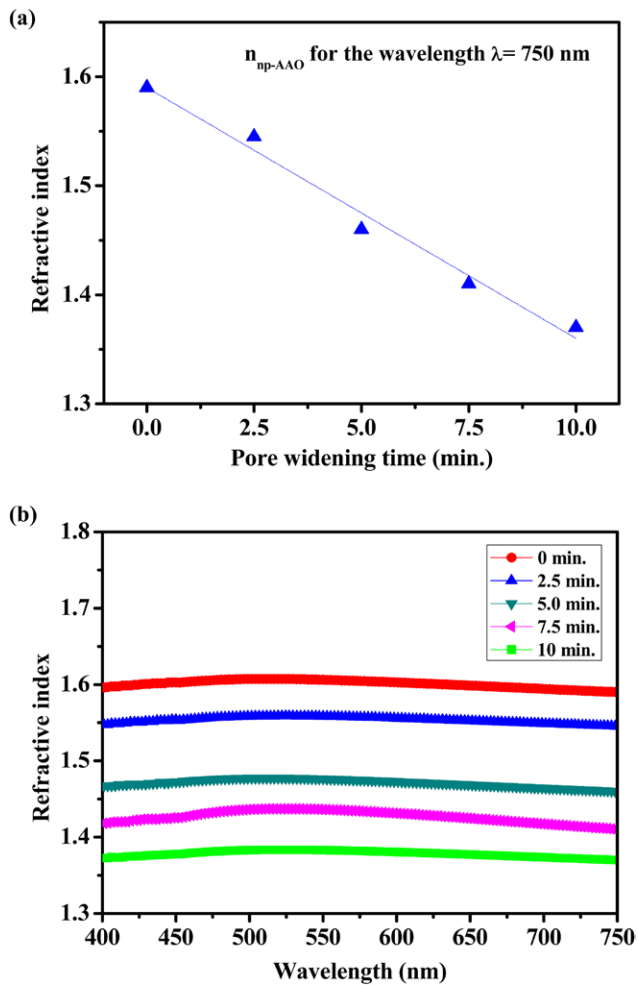


**Figure 6.** (a) Effective refractive index of np-AAO film for the wavelength  $\lambda = 750$  nm, and (b) refractive index dispersion curves of np-AAO films for 0 to 10 min pore-widening time.

electrical properties and is found to be a promising material for the bi-stable modulation thin film optical filter.

### 3. Fabrication and results

The schematic fabrication process steps of the current optical thin film filter are illustrated in figure 4. The substrate used for the fabrication of the presented device was a p-type (0.001–0.005 ohm-cm resistivity) (100) silicon wafer. As indicated in figure 4(a), the  $1\mu\text{m}$  thermal oxide and  $0.5\mu\text{m}$  poly-Si were deposited to respectively act as the etch-stop and sacrificial layers. Thus, the air gap of the optical device was defined by the thickness of the sacrificial layer. Moreover, the  $0.5\mu\text{m}$  Al film was also deposited for the fabrication of the np-AAO layer. After that, the AAO layer with nanopore arrays was grown via a two-step anodization process [29], as shown in figures 4(b)–(d). During the first anodization process shown in figure 4(b), the wafer was first immersed in the  $7^\circ\text{C}$  aqueous solution with 0.3M oxalic acid at a 40V dc input voltage and then the np-AAO layer was formed on the surface of the Al film. As illustrated in figure 4(c), the np-AAO

layer formed in the first Al anodization was removed by the mixture of chromic acid (1.8 wt%) and phosphoric acid (6 wt%) at  $70^\circ\text{C}$ . Subsequently, the nanopore morphology was created on the surface of Al film to enable the growing of new porous alumina with a more regular structure during the second anodization process displayed in figure 4(d). The process condition for the second anodization was the same as that of the first. The pores of the np-AAO layer were then widened using the 5 wt% phosphoric acid at  $27^\circ\text{C}$ , as shown in figure 4(e). The process was not only for the pore widening but also for the final removal of the hemispherical structure at the bottom of the pore columnar structure [30]. Thus, the size of the nanopores was determined in this process to meet the requirements for optical characteristics and anti-stiction. In summary, the processing parameters for the two-step anodization, such as applying voltage, temperature and time for anodization were employed to control the size of the nanopore structure, including cell and pore indicated in figure 3(a). As shown in figure 4(f), the np-AAO film was further etched and patterned by the chromic acid to define the shape of the interference layer. As depicted in figure 4(g), a 20 nm Al film was deposited and patterned onto the np-AAO layer to act as the top electrode and also as the protection layer for the following etching process. As reported in [31], the etching selectivity of Al to poly-Si in  $\text{XeF}_2$  is higher than 1000:1. Thus, the degradation of Al film after the  $\text{XeF}_2$  etching is ignored. Moreover, the Al film with high reflectivity (>90%) over the entire visible spectral range [14] was also employed to enhance the optical reflectivity of the device. Finally, the sacrificial poly-Si was isotropically etched using  $\text{XeF}_2$  gas (dry etching) to suspend the np-AAO layer from the substrate, as shown in figure 4(h). The thermal oxide was employed to protect the Si substrate during the  $\text{XeF}_2$  etching. The stiction of the suspended np-AAO layer with the Si substrate was prevented by the dry etching. Since the nanopores of the np-AAO were covered with Al film, the  $\text{XeF}_2$  could only undercut the poly-Si sacrificial layer from the edge of the device. The etching rate of the poly-Si undercut was not influenced by the size of the nanopores.

The FE-SEM (field emission scanning electron microscopy) images in figure 5(a)–5(c) show the top-view of the np-AAO film. The micrograph in figure 5(a) displays the np-AAO film with a close-packed array of hexagonal cells and nanopores. The nanopore structure with average pore radius ( $r$ ) of  $11 \pm 4$  nm and average interpore distance ( $\rho$ ) of  $85 \pm 6$  nm was implemented after the process in figure 4(d). The micrograph in figure 5(b) displays the np-AAO film after the pore-widening process depicted in figure 4(e). The pore-widening process takes place at the interface between the alumina and the solvent and the pore radius increases linearly with time for a constant reaction speed [30]. After the pore-widening process for 10 min, the average pore radius ( $r$ ) and the interpore distance ( $\rho$ ) become  $28 \pm 5$  and  $91 \pm 6$  nm, respectively. The minor change in the interpore distance could result from the error in the measurements. The FE-SEM image in figure 5(c) shows the np-AAO film covered with the 20 nm Al electrode (reflector) after the process illustrated in figure 4(g). Four-point probe measurements showing the

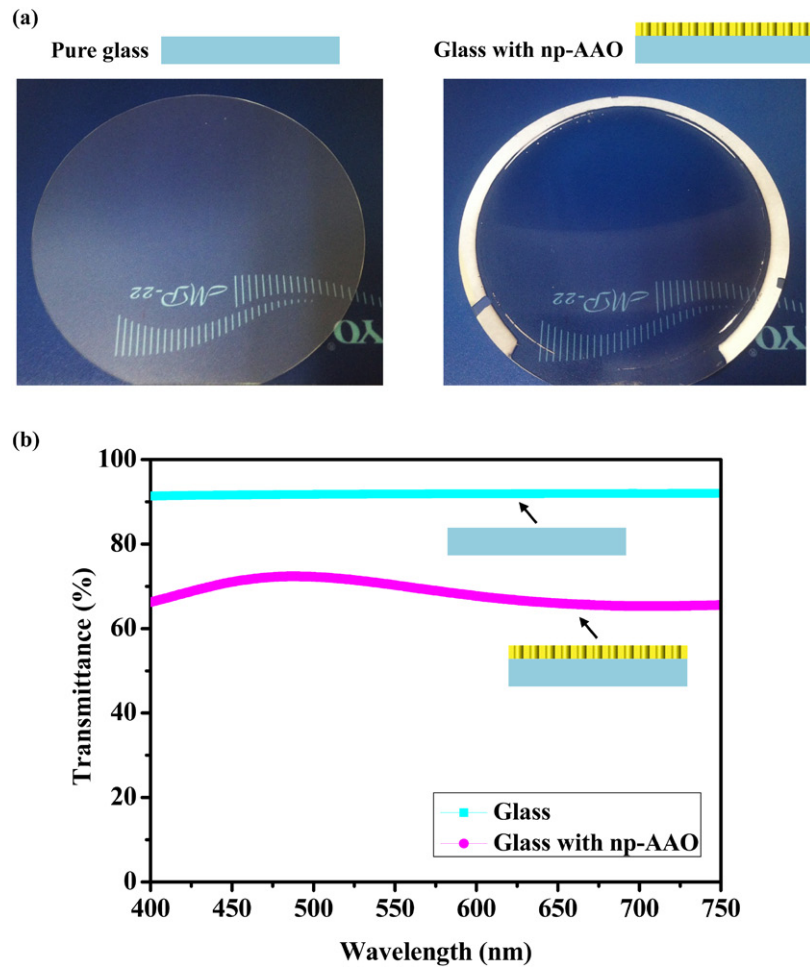


Figure 7. The transmittance of the np-AAO layer for the light beam with wavelength ranging from 400 to 750 nm.

resistivity of 20 nm Al film deposited on top of the np-AAO layer is  $1.2 \approx 2.6 \times 10^{-3}$  ohm cm. In comparison, the resistivity of 20 nm Al film deposited on top of bare Si is  $7.3 \approx 8.1 \times 10^{-4}$  ohm cm. This indicates that the resistivity of Al film is only slightly increased when deposited on np-AAO film. The SEM micrograph in figure 5(d) was taken at the cross section BB' indicated in figure 4(g). This shows the typical layer stacking of the device before the removal of the sacrificial poly-Si film. The np-AAO film with the close-packed array of columnar cells and nanopores can be observed. The micrograph in figure 5(e) was taken at the device edge CC' indicated in figure 4(h). It further shows the cross section view of the np-AAO layer suspended above the substrate after the sacrificial poly-Si film was etched away, as indicated in the process figure 4(h). Note that the shape of the np-AAO interference layer was defined by the wet etching of chromic acid (figure 4(f)). Thus, the columnar cells at the edge of the device (such as CC' in figure 4(h)) were attacked by the chromic acid during wet etching in this step. However, the columnar cells inside the device (such as BB' in cross section figure 4(g)) were protected during the chromic acid wet etching. As a result, the columnar cells are clearly observed in figure 5(d) as compared with figure 5(e). The air gap between the suspended np-AAO layer and the oxide film on the substrate was

0.5 μm. Moreover, the micrograph in figure 5(f) shows the morphology of the back side of the np-AAO film. Based on the image-processing software ImageJ (National Institutes of Health, USA), the porosity of np-AAO film was determined. The solid alumina and nanopores respectively became light and dark areas after image processing and thus the porosity was determined by software. In this case, the porosity at the back side of the np-AAO is 43%. As a reference, the front side of this np-AAO layer has a porosity of 58%. There are two reasons for the difference in the porosity between the front side and back side of the np-AAO layer: (1) some of the nanopores are not successfully etched through, and (2) the size (diameter) of the back side nanopore is smaller than that of the front side.

#### 4. Experiments and discussions

In this study, the wavelength of light is much larger than the pore size and the distance between the pores, hence the np-AAO can be considered as a uniform layer with an effective refractive index [32, 33]. The effective refractive index of np-AAO film was measured by the ellipsometer. The measurements in figure 6(a) show the variation of the effective

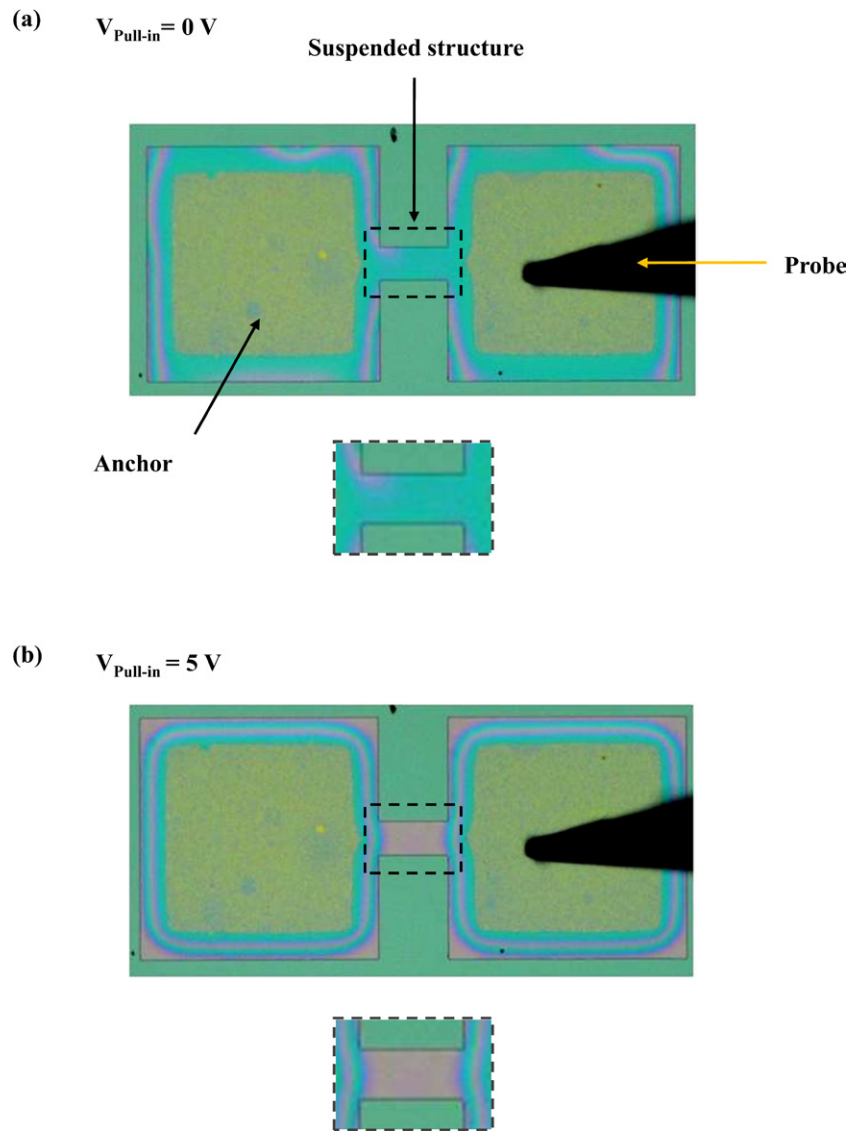


**Figure 8.** Two colors displayed by the bi-stable optical filter at its on-off states modulated by driving voltages.

refractive index  $n$  with the nanopore size of np-AAO film for the wavelength of 750 nm. The np-AAO film consists of the alumina ( $n_{\text{Al}_2\text{O}_3} = 1.8$ ) and the air ( $n = 1$ ) inside the pores. As discussed in equation (2), the refractive index of np-AAO  $n_{\text{AAO}}$  will be modulated by the porosity  $P$ . Measurements indicate the porosity  $P$  was increased from 21% to 58% after the 10 min pore-widening process and then the refractive index was decreased from 1.59 to 1.37. Figure 6(b) further shows the refractive index dispersion curves (in the visible spectral region between 400 to 750 nm) of np-AAO films for 0 to 10 min pore-widening time (i.e. porosity ranging from 21% to 58%). The transmittance of np-AAO is of importance for the application of the optical filter. Figure 7 shows the transmittance of the np-AAO layer for the light beam with wavelength in the visible spectral region between 400 to 750 nm. Figure 7(a) shows the samples, pure glass substrate and glass substrate with np-AAO coating, prepared in this study for measurements. The data in figure 7(b) was measured by using the UV-visible spectrometer (Oceanoptics, model

ISS-UV-VIS and USB2000) with the transmittance of air as the reference. The transmittance of the glass substrate, as indicated in the left photo shown in figure 7(a), is around 90%. In comparison, the transmittance of glass substrate with 350 nm thick np-AAO film (anodized at a bias voltage of 40 V) almost reaches 70%. The data shows that the np-AAO film has good transparency in the visible spectral region.

The micrographs in figure 8 respectively show two colors displayed by the bi-stable optical filter. As marked by dash line in the figure, the optical filter is a suspended np-AAO beam with planar dimensions of  $110 \times 50 \mu\text{m}$ . As shown in figure 8(a), the optical filter displays the green color when no voltage is applied to the device. In addition, as shown in figure 8(b), the np-AAO beam displays the red color when applying 5 V dc voltage (exceeds the pull-in voltage) on the device. Thus, the color filter modulated by the voltage is demonstrated. In brief, the bi-stable states of the suspended beam modulated by the driving voltages enable the change of displayed color. The experimental setup in figure 9(a) was established to measure

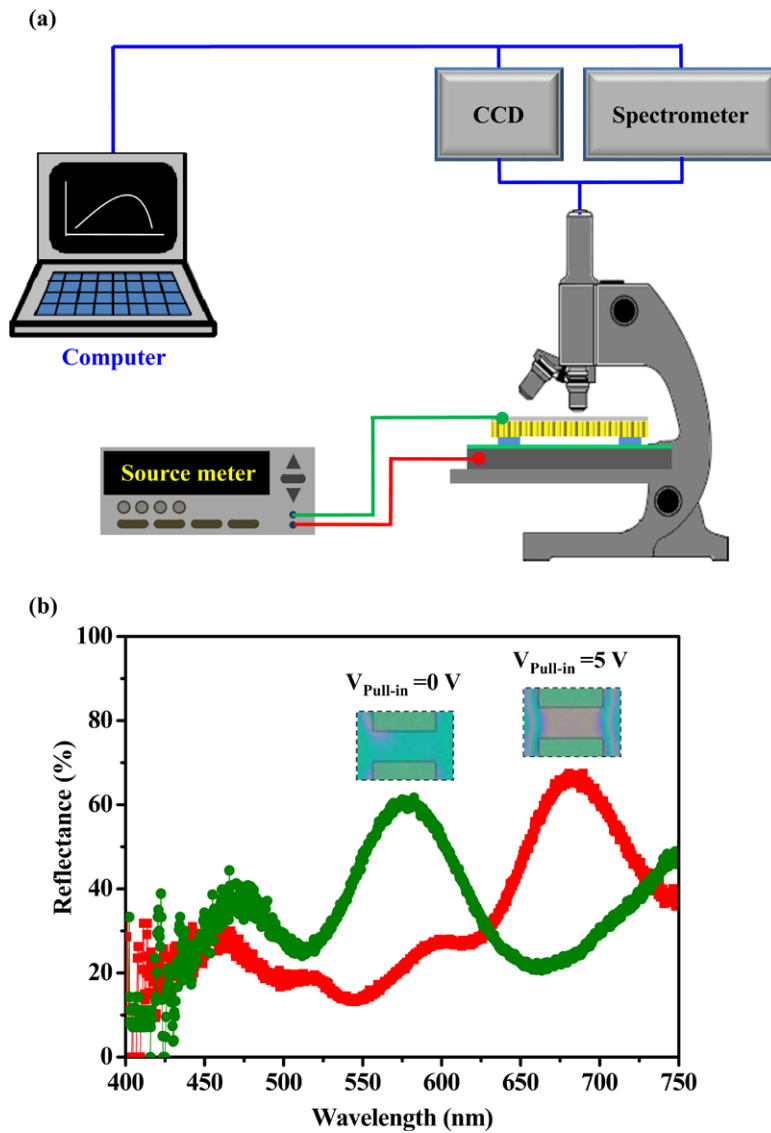


**Figure 9.** (a) Experimental setup for optical spectral measurement and (b) typical measured reflectance of the presented optical filter.

the spectral of light beam reflected from the presented optical thin film filter. The setup consists of the microscope, spectrometer, source meter and the test sample. The source meter was used to apply a dc voltage to deform the suspended thin film filter. The white light from the microscope was incident perpendicularly onto the sample and then the light reflected from the filter was measured by the spectrometer. In addition, the light reflected from the Si with 500nm Al coating film was used as a reference. Figure 9(b) shows the typical measured reflectance of the presented optical filter device. It indicates the relationship between the applied voltages and the light reflectance at different wavelengths. The peak wavelength of light reflectance shifted from 580nm (green) to 690nm (red) as the applied voltage increased from 0 to 5V. These two peak wavelengths are respectively associated with the bi-stable states of the filter. Moreover, the reflectance for green and red were respectively 61.6% and 67.4%.

The test setup in figure 9(a) was also used to characterize the hysteresis curves of a typical fabricated filter. In this

test, the reflected light intensity was detected by the charge-coupled device (CCD) camera. Thus, the variation of the input driving voltage with the reflected light intensity was recorded by computer. The optical filter respectively displays the green color (for no driving voltage) and red color (after the applied driving voltage), as shown in figure 8. Thus, the red light intensity measured by the CCD was exploited to characterize the electrostatic deformation of the suspended thin film. The measurement results in figure 10(a) show the variation of normalized red light intensity with the driving voltage. The driving voltage (positive bias) was increased from 0 to 10V with a 0.4V increment and then decreased from 10 to 0V. Similarly, the driving voltages with negative bias were also applied to the thin film filter. As indicated in the figure, the positive and negative pull-in voltages are respectively  $V_{\text{pull-in}}^+ = 4.4 \text{ V}$  and  $V_{\text{pull-in}}^- = -3.2 \text{ V}$ . According to [1], the offset voltage determined from  $V_{\text{offset}} = 0.5 \times (V_{\text{pull-in}}^+ + V_{\text{pull-in}}^-)$  is  $V_{\text{offset}} = +0.6 \text{ V}$ . For an ideal dielectric layer with no electric charge during electrostatic actuation, the offset voltage is  $V_{\text{offset}} = 0 \text{ V}$ . On the

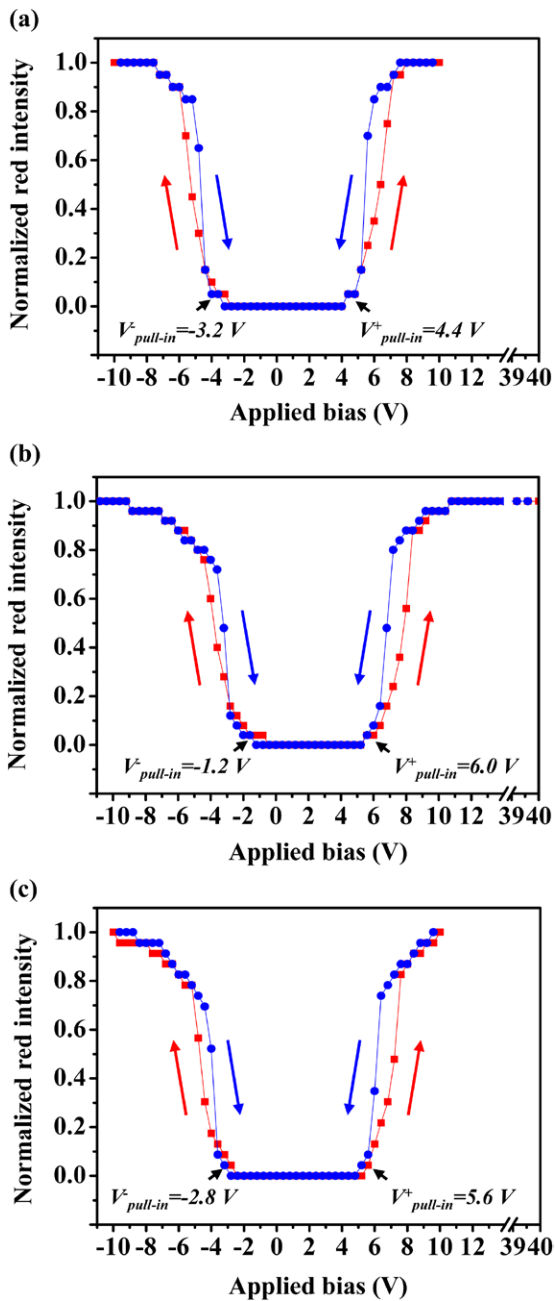


**Figure 10.** Hysteresis curves characterizations for the optical filter device, the results are measured at different test conditions, (a) positive bias from 0 to 10 to 0V and then negative bias from 0 to 10 to 0V, (b) positive bias from 0 to 40 to 0V and then negative bias from 0 to 40 to 0V and (c) positive bias from 0 to 10 to 0V and then negative bias from 0 to 10 to 0V on the sample in (b), the measurement is 1h after the high voltage test.

other hand, the dielectric charge, which will lead to an offset voltage ( $V_{\text{offset}} \neq 0\text{V}$ ) and the hysteresis curves (for positive-bias and negative-bias driving) in figure 10(a) become asymmetric. To evaluate the charges of the dielectric layer, the thin film filter was driven at 40V for 10 min [34]. Such a high applied voltage will lead to the charges being trapped in the dielectric layer. As shown in figure 10(b), the measurements indicate that the offset voltage was increased to  $V_{\text{offset}} = +2.4\text{V}$  ( $V_{\text{pull-in}}^+ = 6.0\text{V}$  and  $V_{\text{pull-in}}^- = -1.2\text{V}$ ). Thus,

the hysteresis curve was shifted to the right due to the existing positive charge [35]. The charge will gradually disappear after a period of time [36]. The measurements in figure 10(c) show the hysteresis curves of the thin film filter after 1h the high voltage tests in figure 10(b). The results indicate that the offset voltage was decreased to  $V_{\text{offset}} = +1.4\text{V}$  ( $V_{\text{pull-in}}^+ = 5.6\text{V}$  and  $V_{\text{pull-in}}^- = -2.8\text{V}$ ) and the hysteresis curves shifted back slightly to the left. In comparison, the  $\text{SiO}_2$  dielectric layer has a  $V_{\text{offset}}$  shifted from 0 to +6V at an applied voltage of 35 V [36]. Moreover, the  $V_{\text{offset}}$  of  $\text{Si}_3\text{N}_4$  dielectric layer is shifted from 0 to +30V at an applied voltage of 65V [33]. As a result, the measurements in figure 10 indicate the np-AAO material has a relatively small dielectric charge as compared with other dielectric materials. The driving voltage (near 5V) for the presented filter design is too small to introduce the dielectric charge. The measurements indicate device design flexibilities and possibilities for higher driving voltage and smaller device size.

The tests and results in figure 11 are employed to investigate the adhesion forces of np-AAO film and oxide during contact. The measurements were performed by using the atomic force microscope (AFM [37, 38]). Figure 11(a) shows the steps to prepare the sample for testing. The np-AAO layer was released from the substrate after the anchor was fully removed by  $\text{XeF}_2$  after etching. After that, the np-AAO film peeled off from the substrate was placed upside down onto another silicon wafer with a thin adhesive layer. After the adhesive layer was cured at room temperature, the sample was ready for AFM adhesion tests. Thus, the AFM tip could touch the contact surface of the np-AAO during the test. Moreover, to investigate the real contact condition (back side of the np-AAO layer to  $\text{SiO}_2$  film), the commercial AFM probe (offered by NT-MDT Co, Russia) with a spherical  $\text{SiO}_2$  fixed on the tip was employed for the adhesion tests. As the SEM micrograph in figure 11(a) shows, the AFM probe has a spherical  $\text{SiO}_2$  with a radius-of-curvature of 650 nm (Model number CSG30\_Bio650). Based on the approach in [37, 38], the AFM tip is initially placed on top of the sample (no contact) and then moves downward to approach and make contact with the sample. An additional loading of the tip is specified to ensure a sufficient contact force between the tip and sample. After that, the AFM tip moves upward to retract from the sample. During the retraction step, the loading between the sample and AFM tip will be gradually decreased to zero as the tip moves back to the initial contact point. However, due to the existence of adhesion force, the cantilever of AFM will remain bent and even retract after the initial contact point. Thus, the adhesion force is determined by the extra load to separate the AFM tip from the sample. Figures 11(b) and (c) show the typical measurement results for np-AAO films of different pore size at an ambient relative humidity of 65%RH. Figures 11(b) respectively indicate the force-displacement measurements for np-AAO film with porosity of 3.6% and 48.2%. The adhesion forces determined from this approach are respectively 80.4 nN (for porosity of 3.6%) and 43.6 nN (for porosity of 48.2%). This shows that the adhesion force was significantly reduced (1.8-fold) by increasing the size of the np-AAO nanopores to prevent the stiction. This study also performed the adhesion

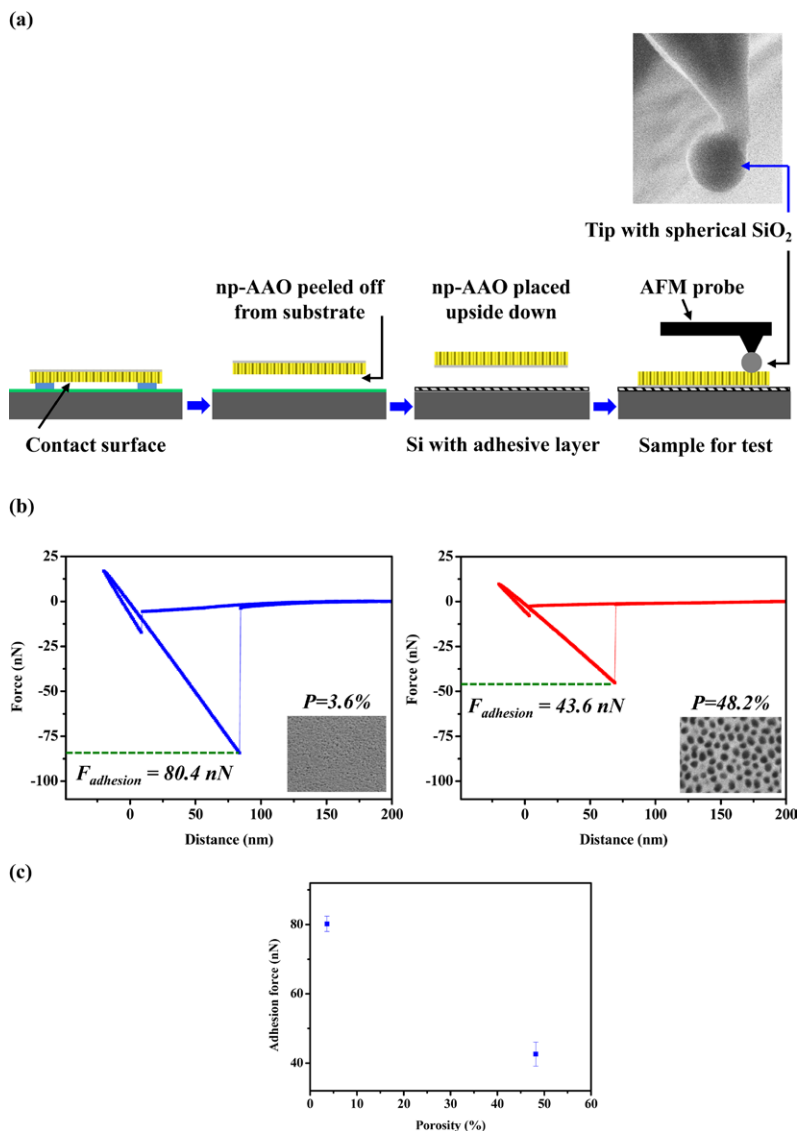


**Figure 11.** Adhesion force test by AFM: (a) the steps for sample preparation, (b) typical force-displacement measurements for np-AAO films of difference pore size, and (c) adhesion tests in five different positions of the sample.

tests in five different positions of the sample and the average adhesion force and the error bar for these measurements are indicated in figure 11 (c). In summary, the adhesion forces determined from this approach are respectively  $80.2 \pm 2.2 \text{ nN}$  (for porosity of 3.6%) and  $42.6 \pm 3.5 \text{ nN}$  (for porosity of 48.2%). Finally, the reliability of the thin film filter was evaluated using the continuous on-off driving tests. The thin film structure was driven by the periodic on-off voltage of 0/10V to ensure its contact with the substrate surface for color modulation. The actuation frequency is 1.6Hz. The measurements in figure 12 show the red-light intensity recorded by the CCD camera during the modulation of the thin film filter for 1 million cycles (almost 180h). The thin film filter displays green and red color at the driving voltages of 0V and 10V, respectively. Thus, the measured red-light intensities are modulated at two different magnitudes at 0V and 10V driving voltages. As stiction of thin film filter occurred, the red light intensity modulation in figure 12 would stop. As a result, no stiction of suspended np-AAO film was observed after driving for

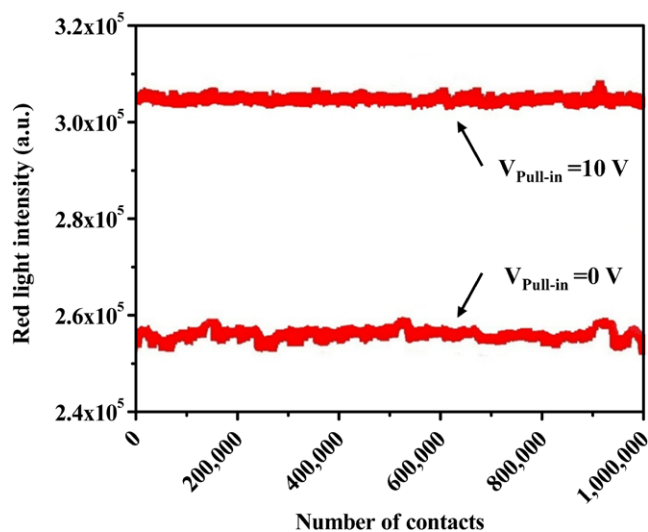


**Figure 12.** Reliability of the thin film filter for continuous on-off driving tests of 1 million cycles.

more than 1 million cycles. The driving tests on unpackaged np-AAO filter were performed to evaluate the influence of the device when exposed to the air. The np-AAO filters were exposed to the air for 2 years. Note that these filters were stored in a chamber with a relative humidity of 45%. The test results show that the driving voltages and the hysteresis curves of these devices remain unchanged.

## 5. Conclusions

This study presents the approach to implement the thin film optical filter by using the suspended np-AAO layer as the key deformable mechanical structure. The thin film filter is driven by electrostatic force with bi-stable positions to modulate the display light of visible wavelength range. The porosity of the np-AAO layer can be exploited to change the characteristics of thin film filter. In this study, the np-AAO with porosity ranging from 21%–58% is demonstrated using the low temperature pore-widening process. Thus, the refractive index can be easily changed from 1.59 to 1.37. The light reflected from the filter is shifted from 580 nm (green) to 690 nm (red) after the bi-stable modulation with a bias voltage of 5 V. Furthermore, the dielectric charge and related offset voltage of the np-AAO filter have been evaluated by the measured hysteresis curves. It indicates that np-AAO film has a relatively small dielectric charge as compared with the SiO<sub>2</sub> and Si<sub>3</sub>N<sub>4</sub> dielectric materials. The experiments further demonstrate that the adhesion force can be reduced by the nano-texture of the np-AAO layer to prevent the in-use stiction of the thin film filter. The device remains alive and no stiction occurred after the on/off bi-stable actuation of 1 million cycles. In summary, the np-AAO is found to be a promising material for electrostatic actuation film optical filters. Moreover, the np-AAO could also find applications in other micro electrostatic drive devices (such as micro switches) based on its superior material properties.

## Acknowledgments

This paper was partially supported by the Brain Research Center at the National Tsing Hua University, and by the National Science Council, Taiwan, under contract 103N2061E1 and NSC 101-2221-E-007-069-MY3. The authors also gratefully acknowledge the National Tsing Hua University (Taiwan) for providing fabrication facilities.

## References

- [1] Felhofer D, Khazeni K, Mignard M, Tung Y J, Webster J R, Chui C and Gusev E P 2007 Device physics of capacitive MEMS *Microelectron. Eng.* **84** 2158–64
- [2] Lo C Y, Huttunen O H, Hiitola-Keinanen J, Petaja J, Fujita H and Toshiyoshi H 2010 MEMS-controlled paper-like transmissive flexible display *J. Micro-Electron. Syst.* **19** 410–8
- [3] Chui C *et al* 2007 The iMoD display: considerations and challenges in fabricating MOEMS on large area glass substrates *Proc. SPIE* **6466** 646609
- [4] Yamanoi T, Endo T and Toshiyoshi H 2008 A hybrid-assembled MEMS Fabry–Perot wavelength tunable filter *Sensors Actuators A* **145–146** 116–22
- [5] Aratani K, French P J, Sarro P M, Poenar D, Wolffenbuttel R F and Middelhoek S 1994 Surface micromachined tuneable interferometer array *Sensors Actuators A* **43** 17–23
- [6] Blomberg M, Kattelus H and Miranto A 2010 Electrically tunable surface micromachined Fabry–Perot interferometer for visible light *Sensors Actuators A* **162** 184–8
- [7] Correia J H, Bartek M and Wolffenbuttel R F 1999 Bulk-micromachined tunable Fabry–Perot microinterferometer for the visible spectral range *Sensors Actuators A* **76** 191–6
- [8] Wolffenbuttel R F 2005 MEMS-based optical mini- and microspectrometers for the visible and infrared spectral range *J. Micromech. Microeng.* **15** S145–52
- [9] Fernandes A V, Cardoso V F, Rocha J G, Cabral J and Minas G 2008 Smart-optical detector CMOS array for biochemical parameters analysis in physiological fluids *IEEE Trans. Indust. Electron.* **55** 3192–200
- [10] Li M, Wang M and Li H 2006 Optical MEMS pressure sensor based on Fabry–Perotinterferometry *Opt. Express* **14** 1497–504
- [11] Jaibir S, Nagendra K and Amitava D 2012 Fabrication of low pull-in voltage RF MEMS switches on glass substrate in recessed CPW configuration for V-band application *J. Micromech. Microeng.* **22** 025001
- [12] Zou M, Wang H, Larson P R, Hobbs K L, Johnson M B and Awitor O K 2006 Ni nanodot-patterned surfaces for adhesion and friction reduction *Tribol. Lett.* **24** 137–42
- [13] Puurunen R L *et al* 2011 Reducing stiction in Microelectromechanical Systems by nanometer-scale films grown by atomic layer deposition *Transducers'11 (Beijing, China, 5–9 June 2011)* pp 1887–90
- [14] Bartek M, Correia J H and Wolffenbuttel R F 1999 Silver-based reflective coatings for micromachined optical filters *J. Micromech. Microeng.* **9** 162–5
- [15] Kumeria1 T and Losic D 2012 Controlling interferometric properties of nanoporous anodic aluminium oxide *Nanoscale Res. Lett.* **7** 88
- [16] Lo P H, Lee C C and Fang W 2012 Implementation of electrostatically controlled Fabry–Perot interferometer using nanoporous anodic aluminum oxide layer *Transducers'13 (Barcelona, Spain, 16–20 June 2012)* pp 677–80
- [17] Trezza M, Cirillo C, Vorobjeva A I, Outkina E A, Prischepa S L and Attanasio C 2013 Vortex matching effects in Nb thin films due to Ni nanopillars embedded in anodic aluminum oxide substrates *Nanotechnology* **26** 035001
- [18] Perego D, Franz S, Bestetti M, Cattaneo L, Brivio S, Tallarida G and Spiga S 2013 Engineered fabrication of ordered arrays of Au–NiO–Au nanowires *Nanotechnology* **24** 045302
- [19] Kim D H, Kim Y, Kim B M, Ko J S, Cho C R and Kim J M 2011 Uniform super hydrophobic surfaces using micro/nano complex structures formed spontaneously by a simple and cost-effective nonlithographic process based on anodic aluminum oxide technology *J. Micromech. Microeng.* **21** 045003
- [20] Cha K J, Na M H, Kim H W and Kim D S 2014 Nano Petri dishes: a new polystyrene platform for studying cell-nanoengineered surface interactions *J. Micromech. Microeng.* **24** 055002
- [21] Wang Z, Sun T, Wang L, Zuo Q, Zhao Y, Xu Z and Liu W 2012 Application of multi-mask layers for high aspect ratio soft mold imprint *J. Micromech. Microeng.* **22** 125025
- [22] Gong S H S, Stolz A, Myeong G H, Dogheche E, Gokarna A, Ryu S W, Decoster D and Cho Y H 2011 Effect of varying pore size of AAO films on refractive index and birefringence measured by prism coupling technique *Opt. Lett.* **36** 4272–4

- [23] Macleod H A 1986 *Thin-Film Optical Filters* 2nd Ed (MacMillan: New York)
- [24] Choi D, Lee S, Lee C, Lee P, Lee J, Lee K H, Park H and Hwang W 2007 Dependence of the mechanical properties of nanohoneycomb structures on porosity *J. Micromech. Microeng.* **17** 501–8
- [25] Zhuo H, Peng F, Lin L, Qu Y and Lai F 2011 Optical properties of porous anodic aluminum oxide thin films on quartz substrates *Thin Solid Films* **519** 2308–12
- [26] Kaajakari V 2009 *Practical MEMS: Analysis and Design of Microsystems, MEMS Sensors, Electronics, Actuators, RF MEMS, Optical MEMS, and Microfluidic Systems* (Las Vegas: Small Gear Publishing)
- [27] Li A P, Müller F, Birner A, Nielsch K and Gösele U 1998 Hexagonal pore arrays with a 50–420 nm interpore distance formed by self-organization in anodic alumina *J. Appl. Phys.* **84** 6023–6
- [28] Moreno-Hagelsieb L, Flandre D and Raskin J R 2009 Mechanical properties of anodic aluminum oxide for microelectromechanical system applications *J. Vac. Sci. Technol. B: Microelectron. Nanometer Struct.* **27** 542–6
- [29] Masuda H, Yamada H, Satoh M, Asoh H, Nakao M and Tamamura T 1997 Highly ordered nanochannel-array architecture in anodic alumina *Appl. Phys. Lett.* **71** 2770–72
- [30] Jung Y W, Byun J S, Woo D H and Kim Y D 2009 Ellipsometric analysis of porous anodized aluminum oxide films *Thin Solid Films* **517** 3726–30
- [31] Chang F I, Yeh R, Lin G, Chu P B, Hoffman E, Kruglick E J, Pister K S J, and Hecht M H 1995 Gas-phase silicon micromachining with xenon difluoride *Proc. SPIE*, **2641** 117–28
- [32] Saito M and Miyagi M 1989 Anisotropic optical loss and birefringence of anodized alumina film *J. Opt. Soc. Am.* **6** 1895–900
- [33] Aspnes D E, Theeten J B and Hottier F 1979 Investigation of effective-medium models of microscopic surface roughness by spectroscopic ellipsometry *Phys. Rev. B* **20** 3292–302
- [34] Herfst R W, Huizing H G A, Steeneken P G and Schmitz J 2006 Characterization of dielectric charging in RF MEMS capacitive switches *Proc. of IEEE Int. Conf. on Microelectronic Test Structures (6–9 March 2006)* pp 133–6
- [35] Herfst R W, Steeneken P G and Schmitz J 2007 Time and voltage dependence of dielectric charging in RF MEMS capacitive switches *Proc. of IEEE 45th Annu. Int. Reliab. Phys. Symp. (Phoenix, Az, 15–17 April 2007)* pp 417–21
- [36] Wolf I D, Czarnecki P, Jourdain A, Modlinski R, Tilmans H, Puers R, van Beek J and van Spengen W M 2005 The influence of the package environment on the functioning and reliability of capacitive RF-MEMS switches *Microw. J.* **48** 102–16
- [37] Maboudian R and Howe R T 1997 Critical Review: Adhesion in surface micromechanical structures *J. Vac. Sci. Technol. B* **15** 1–20
- [38] Jones R, Pollock H M, Geldart D and Verlinden A 2003 Interparticle forces in cohesive powders studied by AFM: effects of relative humidity, particle size and wall adhesion *Powder Technol.* **132** 196–10